LA-UR-16-24195 (Accepted Manuscript)

Theoretical neutron damage calculations in industrial robotic manipulators used for non-destructive imaging applications

Hashem, Joseph Anthony
Schneider, Erich
Pryor, Mitch
Landsberger, Sheldon

To be published in: Progress in Nuclear Energy

DOI to publisher's version: 10.1016/j.pnucene.2016.09.022

Permalink to record: http://permalink.lanl.gov/object/view?what=info:lanl-repo/lareport/LA-UR-16-24195

Theoretical neutron damage calculations in industrial robotic manipulators used for non-destructive imaging applications

Joseph Hashem[a, b, *]
jhashem@lanl.gov

Erich Schneider[b]

Mitch Pryor[b]

Sheldon Landsberger[b]

[a]Los Alamos National Laboratory, P.O. Box 1663, Los Alamos, NM 87545, USA

[b]University of Texas at Austin, Austin, TX 78712, USA

*Corresponding author. Los Alamos National Laboratory, P.O. Box 1663, Los Alamos, NM 87545, USA.

Abstract
This paper describes how to use MCNP to evaluate the rate of material damage in a robot incurred by exposure to a neutron flux. The example used in this work is that of a robotic manipulator installed in a high intensity, fast, and collimated neutron radiography beam port at the University of Texas at Austin's TRIGA Mark II research reactor. This effort includes taking robotic technologies and using them to automate non-destructive imaging tasks in nuclear facilities where the robotic manipulator acts as the motion control system for neutron imaging tasks. Simulated radiation tests are used to analyze the radiation damage to the robot. Once the neutron damage is calculated using MCNP, several possible shielding materials are analyzed to determine the most effective way of minimizing the neutron damage. Neutron damage predictions provide users the means to simulate geometrical and material changes, thus saving time, money, and energy in determining the optimal setup for a robotic system installed in a radiation environment.

Keywords: Neutron radiation damage; MCNP; Radiography; Non-destructive testing; Robotics; Research reactor

1 Introduction

Penetrating radiation has been used throughout history for imaging purposes dating back to 1895 when Roentgen discovered x-rays. Emerging threats to national security from cargo containers and improvised explosive devices have reinvigorated efforts using tomography and compact radiography. Additionally, unusual environmental threats, like those from underwater oil spills and nuclear power plant accidents, have caused renewed interest in fielding radiography in severe operating conditions. Today any particle type can be combined with an increasingly wide range of digital detectors to image almost any conceivable object in extreme environments. These severe operating conditions pave the way for remote handling systems, such as robots, where they are increasingly deployed in remote and hazardous environments such as in nuclear waste cleanup and other radioactive environments. The DOE has in particular targeted robotic handling of hazardous waste to be an essential element in its efforts of environmental restoration and waste management (DOE, 1990). Within the DOE complex, the primary purpose of robots are to replace (or augment) human operators to increase safety without adversely impacting process efficiency.

In this work, a Yaskawa SIA5 7 Degree-of-Freedom (DoF) industrial manipulator (YASKAWA, 2012) handled the imaged parts and provided advanced and flexible motion capabilities and imaging techniques. Remote-operated robots like the one studied here allow access and manipulability to areas that would otherwise be inaccessible due to radiation levels, enabling repairs, maintenance work, inspections, or other tasks. A good example of this is the Fukushima plant in Japan, which is using robotic inspection to determine the extent of damage inside the contaminated reactor buildings (Nagataniet al, 2012). These robotic servants are not invulnerable however, and radiation exposure will result in damage to the components. Monte Carlo tools like MCNP (Goorley et al., 2012) can enable us to easily perform the high-fidelity calculations necessary to determine the neutron damage rate. MCNP provides a powerful tool for determining radiation fields in a defined

environment (Gilbertet al, 2013). High enough levels of neutrons or photons will eventually affect the reliability of electronic components. Thus radiation tolerance is critical to the reliability of the imaging process. Therefore, the radiation damage to the robot and its electronics must be quantitatively evaluated.

Exposure to a radiation field, including neutron flux, leads to damage, including weakening in materials, metal embrittlement, and reduced semiconductor efficiency. The incident radiation carries a certain amount of energy, which is transmitted to the material through various processes (e.g. elastic and inelastic scattering of neutrons). If enough energy is transmitted to an atom of the material, that atom can be displaced from its position in the molecular structure leaving a vacant site behind (vacancy), and the displaced atom eventually comes to rest in a location among lattice sites, becoming an interstitial atom. The interstitial vacancy pair is of main importance for radiation effects in solids and is known as a Frenkel Pair (FP). The presence of the FP and other consequences of irradiation damage determine the physical effects, and with the application of stress, the mechanical effects of irradiation. The radiation damage event is finished when the displaced atom (also known as the primary knock-on atom, (PKA)) comes to rest in the lattice as an interstitial (Was, 2007). As the vacancies, interstitials, and voids caused by repeated displacements build up, the crystalline molecular structure of the material is weakened. For materials like metals and semiconductors, where key properties like material strength and conductivity are highly dependent on the crystalline structure, repeated radiation-induced displacement can severely impact the material's ability to perform its intended function, reducing the service life of any component made of that material.

Monte Carlo methods have been used to determine neutron-induced displacements and radiation damage primarily for reactor vessel applications. At Oak Ridge, Monte Carlo tools were used to assess neutron and photon induced embrittlement in the High Flux Isotope Reactor (HFIR) reactor vessel as demonstrated by Risner and Blakeman (Risner and Blakeman, 2016). A limited evaluation of neutron displacements per atom (DPA) rates at a beam port nozzle corner region at HFIR using a Monte Carlo model was performed in (Blakeman and Bucholz, 2004). DPA rate maps using three-dimensional cylindrical mesh tallies were used to visualize the spatial map of neutron and photon DPA rates. Mascitti and Madariaga (Mascitti and Madariaga, 2011) also implement Monte Carlo tools to identify where the Atucha II reactor pressure vessel neutron radiation from fast neutrons is highest and perform DPA rate calculations in those areas.

The sensitive components installed on advanced manipulators can be divided into three categories: 1) the drives (usually electrical actuators with bearings, gear boxes and position feedback devices); 2) the sensors (distance and force sensors, cameras, etc.); and 3) the cables and other communication devices (including line drivers, multiplexing circuits, analog to digital converters, radio links and even the preamplifiers needed for some sensors). For each category, the radiation hardening level required will depend on their location with respect to the radiation sources (near the end effector or near gantry tracks or walls) and on their frequency of use (e.g., a tool used a small number of times, compared with protection systems in use permanently) (Houssay, 2000). The robot's controller can and should be kept out of the radiation environment due to its large amount of electronics.

Potentially, the most radiation sensitive parts of a robotic system are the electronic components. The electronic parts that are the most susceptible to radiation effects are the semiconductors, the semi-insulators, and insulators. The most important of these are the silicon family of parts. Non-semiconductor based electronic and electromechanical components such as servo-motors generally exhibit much greater radiation resistance. For robotic applications in radiation environments, the primary radiation effects of concern are total ionizing dose and the neutron-induced displacement damage. Single event upsets produced by high energy neutrons and space radiation are only of minor importance for the vast majority of robotic applications except for those in space.

1.1 Displacements per atom

A standard parameter in the determination of radiation damage in materials is the displacement per atom (DPA), an integral magnitude that includes information about the material response (displaced atoms) and the neutron fluence (magnitude and spectrum) to which the material was exposed. DPA is not a measure of initially created lattice defects in the material but a measure of the harming energy deposited by neutrons in terms of the number of atoms permanently displaced from their position to a stable interstitial position. DPA is

the magnitude usually used to correlate damage on materials irradiated under different neutron conditions and is the value of interest. The DPA rate is a derived quantity, which can be obtained dividing R, the number of displacements per unit volume and time, by the atomic density N of the material,

$$R_{DPA} = \frac{R}{N} = \frac{\sigma_D \varphi}{2E_D} = \eta_{MC} \frac{R_{D,MC}}{2E_D} \quad \textbf{(1)}$$

where E_D is a certain threshold energy that must be overcome before an atom can be displaced. This threshold energy is fairly small and represents the amount of energy required to overcome the atom's mass and the bonds holding it in place. The displacement cross-section, σ_D, is the product of the number of atomic displacements produced by a radiation particle at a given energy times the differential probability that the radiation particle at that energy level will transfer enough energy to an atom to knock that atom out of its matrix site, integrated over all energies above the displacement threshold. That is, the damage cross-section accounts for both the probability of interaction and the total number of expected interactions across a radiation particle's life. This is unlike most cross-sections, which solely represent the probability of a given interaction occurring. The particle flux is given as φ. MCNP can calculate the cross-section times flux value and provide the damage rate, $R_{D,MC}$. Since this is a computational tool to evaluate the damage rate, an efficiency factor, η_{MC}, accounts for deviations between calculation and reality. The standard efficiency factor for these calculations is 80%, based on binary collision models to account for realistic scattering (Wootan, 2014).

1.2 Application overview

We are going to use MCNP Ver. 6.1 (Goorley et al., 2012) to evaluate the rate of material damage incurred by exposure to a neutron flux. The example we use is that of a remote-operated robot intended for use in high-radiation environments, which is tested using one of the TRIGA beam port facilities. To do this we use macrobodies to create the robot geometry, define composite materials, and use tally multipliers to obtain a specific reaction rate. We discuss each of these features as we develop the model and then look at the specific post-processing needed to get neutron damage results. This work uses the application of a robotic manipulator installed in one of the beam ports at the University of Texas at Austin's (U.T. Austin) TRIGA Mark II research reactor for part placement, manipulation, and exchange for neutron radiography and computed tomography imaging. The use of robots can provide additional flexibility and autonomy to automated non-destructive imaging applications.

1.3 Beam port flux image

The MCNP detector flux pinhole camera tally was used to estimate the flux image at the image plane of the beam port to measure the beam size and beam uniformity. The pinhole size can be adjusted to the region of interest to improve statistics. The FIR tally in MCNP was used to establish a flux image on a rectangular radiograph grid in order to acquire the beam source profiles of Beam Port 5 (BP5) (see Fig. 1), which shows the direct neutron flux at the imaging detector. This tally uses an array of point detectors to measure the flux at various points on a grid. With the grid placed at the imaging plane, variances in the measured flux combined with a color spectrum can generate an image similar to a radiograph. The neutron flux profile of BP5 and the neutron flux density radiograph at the robot/sample position are shown in Fig. 1, both determined using the MCNP model. From Fig. 1 it can be observed that BP5 has a thermalized neutron spectrum and that the neutron flux is more intense in the center of the beam. It can be seen that the flux near the image plane is approximately 40 cm wide on each side and is decreasing by approximately 1/r from the center line of the beam port.

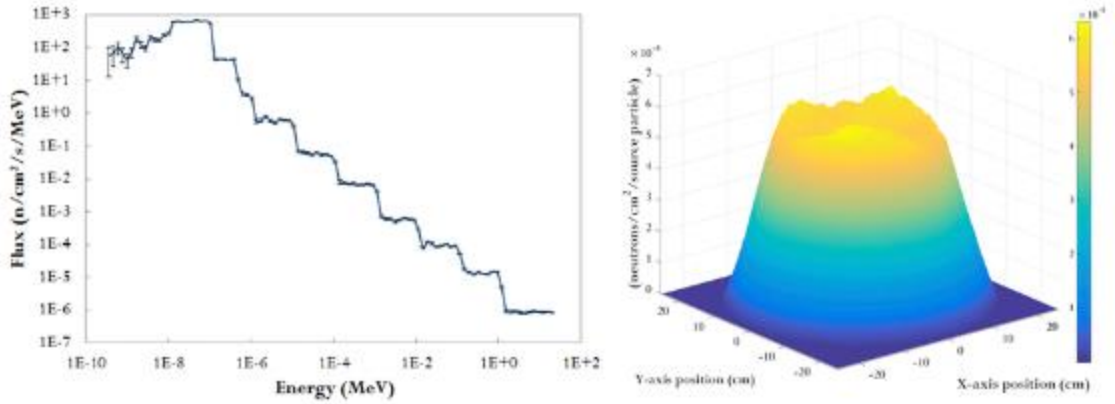

Fig. 1 BP5 thermal neutron energy spectrum (left). BP5 source profile that shows the simulated direct neutron flux image at 2.8 m from the aperture plane (right). This is roughly the flux seen at the imaging plate without the robot or simulated sample in place.

2 Methods

2.1 Imaging system setup

The neutron imaging was performed at one of the tangential channels (BP5) of U.T. Austin's TRIGA Mark II research reactor with a thermal power of 1.1 MW BP5, which was the environment used to calculate neutron damage rates in the robot, has a thermal neutron flux of 2.4×10^6 n/cm^2/s at a reactor power of 950 kW. It is of importance to note that we are dealing with mostly epithermal and thermal neutrons, so high DPA rates are not expected in this example application. A scintillator-mirror-camera system was utilized to acquire digital radiographs. The scintillator used was a copper, aluminum, and gold doped ^{6}LiF ZnS neutron detection screen (Applied Scintillation Technologies, 2014). The reaction that occurs is $^6Li + n \rightarrow {}^4He + {}^3H + 4.8\ MeV$, where the ejected triton interacts with phosphor in the scintillator to create a scintillation event. The camera used was an Andor iXon + EMCCD with an effective pixel pitch of 35 μm (ANDOR Technology, 2008). A stainless steel enclosure, along with lead bricks, surrounded the camera, mirror, and scintillator to shield against x-ray hits and background noise. The experimental setup is shown in Fig. 2. Fig. 3 shows the SIA5 setup in the beam port area with the imaging system.

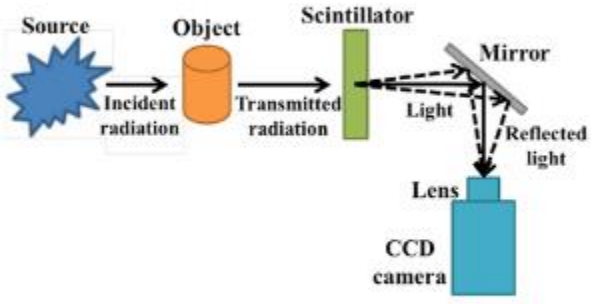

Fig. 2 Schematic of scintillator-mirror-camera radiography system (left). Photograph of image acquisition setup (right).

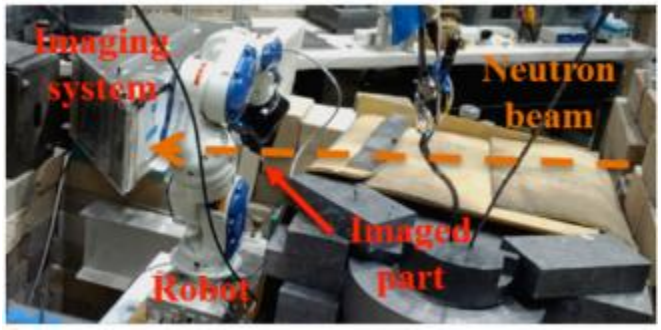

Fig. 3 Photograph of experimental setup with robot placing part in neutron beam for imaging.

2.2 MCNP model geometry and materials description

The MCNP model represents a concrete enclosure built around the terminus of BP5 in the TRIGA reactor. Fig. 4 shows a top-down schematic of the model. The robot is placed at the center of the enclosure,[1]and is represented in the model as a series of three nested cylinders: an 8 cm diameter cylinder (dark blue) representing the internal structure, a 16 cm diameter cylinder representing the shell (light blue), a cylinder of varying thickness representing the shielding (green), and with the total height defined as 70 cm tall.

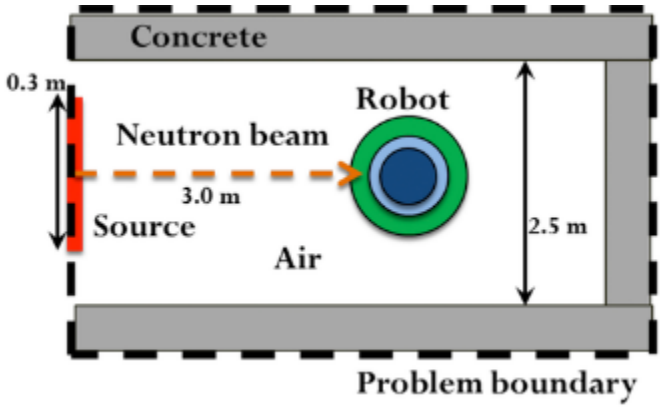

Fig. 4 Top-down view of the simplified BP5 robot neutron damage model. The dark blue circle represents the robot's interior, the light blue circle the robot's exterior shell/casing, and the green circle the shielding around the robot. Not shown to scale.

Knowing specific materials in the robot is important since the damage performance is directly affected by the material type that the neutrons are imparted upon. The shell of the robot is composed of AC4C-T6, an Al alloy with traces of Si, Fe, Cr, and other metals (Kobayashiet al, 1997). The interior is more complicated as it contains cables, wires, actuators, harmonic gears, and other small and geometrically complicated components. Therefore, the interior of the robot is a custom composition representing a homogeneous smear of the various components (10% Si, 5% Cu, 10% Ni, 10% Fe, 5% nitrile rubber, 10% PVC, 15% Delrin, and 35% air). It is important to note that due to lack of accurate information on the exact material details, the material compositions and the densities listed above are estimated based on visual inspection of accessible components and communications with personnel from Yaskawa (Nieves, 2013). The composition of the shielding is the parameter varied; several options were studied, including polyethylene, rubber aluminum, and Fe. A maximum shielding thickness was used for each material with a 2.5 kg weight limit.

MCNP requires materials be broken down into constituents for which cross-sections are available (e.g. elements or isotopes). Most analyses can get away with element-level decomposition. For example, there are no cross-sections for stainless steel, but it can be defined as 70.17% elemental iron, 19% elemental chromium, 9.25% elemental nickel, 1% elemental manganese, and trace elements. However, some cross-section data (like the damage cross sections of interest in this problem) are only available at the isotope level. For example elemental iron would need to be further broken down into 91.75% ^{56}Fe, 5.85% ^{54}Fe, 2.12% ^{57}Fe, and 0.28% ^{58}Fe. For the robot model, there are two composite materials: the robot shell and the robot interior. The robot shell is an aluminum alloy and the interior is a homogeneous smear of multiple materials. Both of these are broken down to the isotopic level to illustrate how complex composite materials can get (Table 1).

Table 1 MCNP composite material definitions for robot shell and robot internal structure.

AC4C-T6 Al alloy for robot exterior		Robot internals composition	
Isotope	Weight fraction	Isotope	Weight fraction
63Cu	0.027668	1H	0.019149
65Cu	0.012332	12C	0.137684
28Si	0.064100	14N	0.270883
29Si	0.003246	16O	0.161070
30Si	0.002155	28Si	0.092330
24 Mg	0.400000	29Si	0.004670
54Fe	0.010521	30Si	0.003100
56Fe	0.165157	35Cl	0.056726
57Fe	0.003814	36Ar	0.004489
58Fe	0.000508	54Fe	0.005845
55Mn	0.040000	56Fe	0.091754
50Cr	0.008690	57Fe	0.002119
52Cr	0.167578	58Fe	0.000282
53Cr	0.019002	58Ni	0.068077
54Cr	0.004730	60Ni	0.026233

AC4C-T6 Al alloy for robot exterior		Robot internals composition	
Isotope	Weight fraction	Isotope	Weight fraction
27Al	0.921900	61Ni	0.001140
		62Ni	0.003634
		64Ni	0.000926
		63Cu	0.034585
		65Cu	0.015415

The neutron beam is emitted from a disk source representing the neutron flux distribution at the terminus of the beam port into a 6 m (length) x 2.5 m (width) x 1.4 m (height) concrete enclosure with 0.4 m thick walls. The neutron source spectrum and emitting direction were determined using another detailed TRIGA Mark II core MCNP model from Young (Young, 1998). Assuming beam line neutrons mainly come from beam scatter, this model was ready to apply to this work. However, it soon became apparent that this detailed model took too long to run to get the results with acceptable accuracy. Therefore such a model was used only to specify the neutron source term for the simplified model used in this paper. To expedite MCNP runtime, the disk source was moved to near the beam exit with a new source spectrum and direction distribution. When dealing with direct contributions to a point detector from a planar surface source, the ARA (area of source) parameter with the SDEF card is required. Fig. 5 shows the thermal neutron energy distribution that is used for the disk source model for BP5. The neutron source definition includes Source Information (SI) and Source Probability (SP) cards to capture the beam port neutron distribution as accurately as possible (Shultis and Faw, 2011). The SI card gives the set or range of values for the variable and the SP card gives the probabilities associated with the values of the SI card.

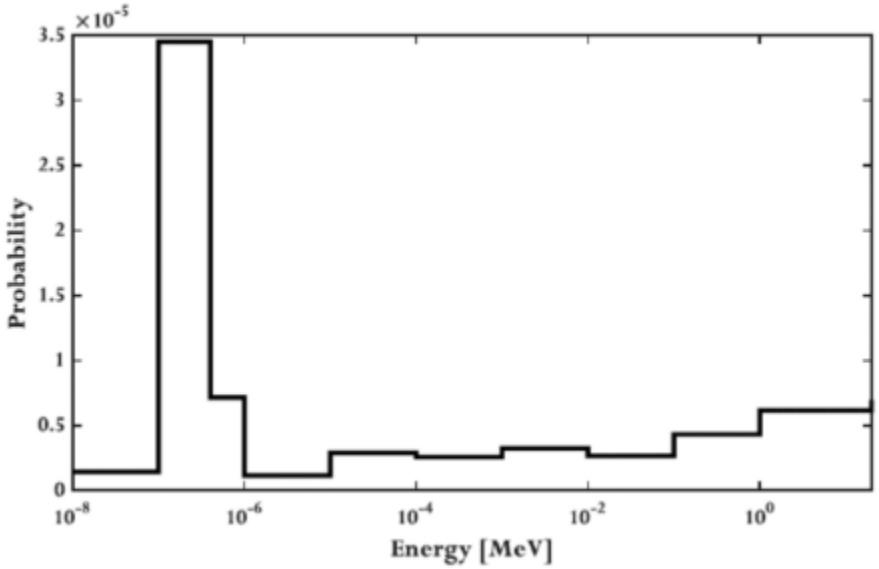

Fig. 5 BP5 thermal neutron source probability histogram.

2.3 Tally information

After the geometry and materials have been specified, MCNP can calculate neutron damage rates. The ACE cross-section library (PyNE, 2016) available for MCNP has neutron damage cross-sections, stored under interaction identifier/reaction number, MT = 444. MCNP can calculate damage rates using an F4 flux tally (Shultis and Faw, 2011) and the damage cross-sections to specify the desired interaction. A flux multiplier card (*FM* card) instructs MCNP to do this using the continuous cross-sections in the ACE library. The *FM* card in this problem is of the form:
FMn c m (rxn list).

where *n* is the user-specified tally number, *c* is a user-supplied multiplicative constant ($c = 1$ in this application), *m* is the material number for which reaction rate is calculated, and *rxn list* is the ENDF reaction type, given by MT numbers. The reaction number for this application is 444. It is possible to rework the FM card to calculate the DPA rate entirely in MCNP. This is implemented by defining the constant, *c*, as $\eta_{MC}/2E_D$, times any time-conversion factor, such as the number of seconds per year. The *FM* card essentially provides a multiplicative factor to be applied to the raw tally results. For this application, the flux passing through a region with a specific cross-section needs to be multiplied to get a reaction rate in that region. MCNP allows one to use any material in the model as the source of the cross-section data. Thus one can define pure elemental materials for each element of interest and supply these materials as the source of the cross-section. This allows the combination of the flux, which is based on the material actually in the region of interest (i.e. the composite material), with a "pure" cross-section, therefore, obtaining reaction rates just for the region and material of interest. These pure materials that are specified for use in tallies only are shown in Table 2.

Table 2 MCNP pure materials specified for use in neutron damage tallies. *Wf* stands for weight fraction.

Pure Al		Pure Si		Pure Fe		Pure Cu		Pure Ni	
Isotope	Wf	Isotope	Wf	Isotope	Wf	Isotope	Wf	Isotope	Wf
27Al	1.0	28Si	0.922	54Fe	0.058	63Cu	0.692	58Ni	0.681
		29Si	0.047	56Fe	0.918	65Cu	0.308	60Ni	0.262
		30Si	0.031	57Fe	0.021			61Ni	0.011
				58Fe	0.003			62Ni	0.036
								64Ni	0.009

There are two regions of interest in the robot, the exterior and interior components. In the outer shell, reaction rates for Al, Si, and Fe are needed, while in the interior of the robot, reaction rates for Si, Fe, Cu, and Ni are needed. The other elements in these regions are either present in low concentrations or are not likely to experience damage (e.g. air). To cover these combinations, seven tallies are required, one tally for each material/region combination. For example, to find the neutron damage rate in Al in the outer shell of the robot, the set of tallies needed are:
F4:N material # for composite AC4C-T6

FM4 (1 material # for pure Al 444)

The resulting tally is the neutron damage rate, or damage cross-section times flux. This result needs to be converted to DPA however. As discussed earlier in this section, DPA is the reaction rate over the threshold energy. Threshold energies for Si, Cu, Al, Ni, and Fe are shown in Table 3.

Table 3 Threshold energies for the materials of interest in this application (Olander, 1975).

Element	Threshold energy (eV)
Si	25
Cu	22
Al	16
Ni	24
Fe	24

3 Results

As mentioned earlier, this work seeks to determine the damage a robot will experience due to exposure to neutron flux. To calculate the DPA rate, Equation (1) is used. It is important to note that the damage rate, R, has units of interactions/sec., the efficiency factor, η_{MC}, is 0.8, and the threshold energy, E_D, can be found from Table 3. MCNP calculates the reaction rates in reactions per second, while damage rates are commonly expressed in DPA per year. Thus, the MCNP values are multiplied by the number of seconds in a year to obtain the results for various shielding types, which are shown in Fig. 6 and Fig. 7 for the exterior and interior of the robot in BP5. It is important to note that all results expressed in terms of DPA/year in this paper actually refer to DPA/effective full-power year, which means that the neutron beam would have to be on the entire year to achieve the resulting DPA values. At these DPA rates, the materials will experience some radiation hardening and embrittlement, which occurs at greater than 0.1 DPA, but changes such as phase instabilities, irradiation creep, and volumetric swelling from void formation will not occur until a DPA value of greater than 10 is achieved (Zinkle, 2012). Note that these results are worst case scenario, with the reactor on for the entire time. Real-world damage rates will be significantly lower since the reactor will not be on the entire year and the robot will not be directly in the beam path the entire time.

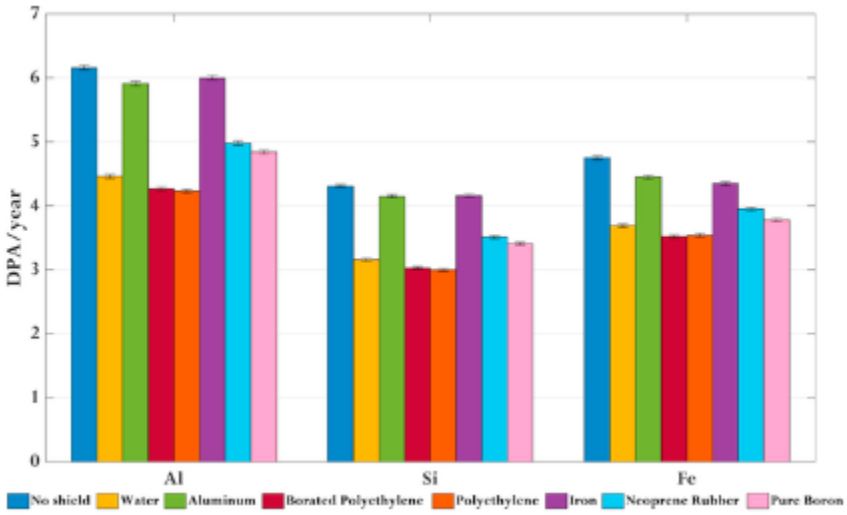

Fig. 6 BP5 outer shell DPA rates and the 1-sigma uncertainties with various shielding materials.

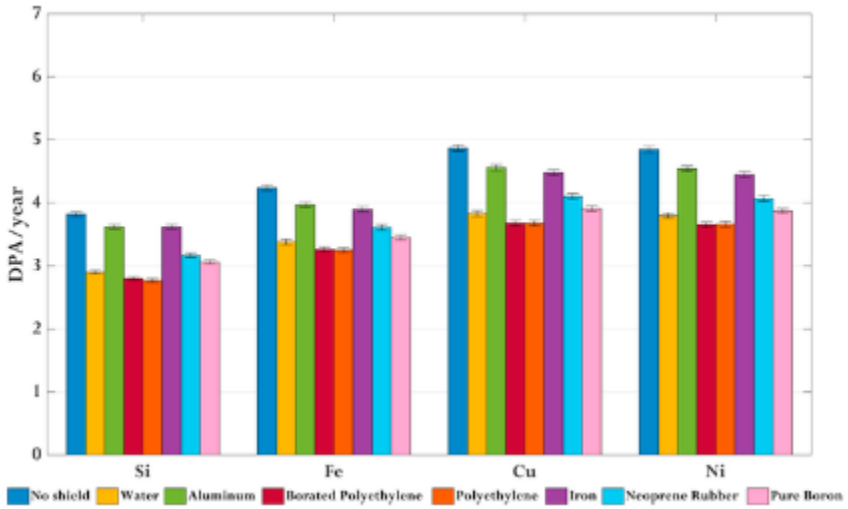

Fig. 7 BP5 interior DPA rates and the 1-sigma uncertainties with various shielding materials.

Polyethylene, as a low-Z material, is the most effective shield. These results include error bars that are based on taking the relative uncertainty from the MCNP tally results and multiplying the DPA/year/MeV by this relative error. The relative error is the fractional 1-sigma estimated uncertainty in the tally mean, i.e. the ratio of the standard deviation of the tally to the mean. This approach assumes that there is no uncertainty in the displacement threshold energy, which is a reasonable approximation. The uncertainty in the results indicates clear distinction between the different types of materials, but it is difficult to resolve between the two polyethylene cases, or between the two metals (i.e. Al and Fe). 500,000 neutron histories are tracked, to achieve a relative uncertainty of roughly 1% or less while maintaining reasonable speed (i.e. the deck runs in about 2 min on a basic laptop).

In Fig. 8 and Fig. 9 the DPA rate in each energy group is plotted as a function of neutron energy for each case in BP5. From Figs. 8 and 9 one can see that as radiation penetrates the robot, the neutron spectrum hardens, reduces the rate of DPA and accordingly decreases the contribution of thermal neutron damage. The DPA rate starts increasing again above energies greater than 200 eV as can be seen in Figs. 8 and 9. This is due to elastic scattering neutron reactions where intermediate and fast neutrons collide and transfer a significant part of its kinetic energy to the scattering nucleus. The total kinetic energy is conserved in elastic scattering of neutrons, and the energy lost by the neutron is transferred to the recoiling nucleus. Also, at higher energies, borated polyethylene is not an effective shielding material. These statements can be translated into numbers observed in Table 4, which present the spectrum of neutron flux and the rate of DPA for six commonly used energy groups for four cases of BP5 mentioned earlier.

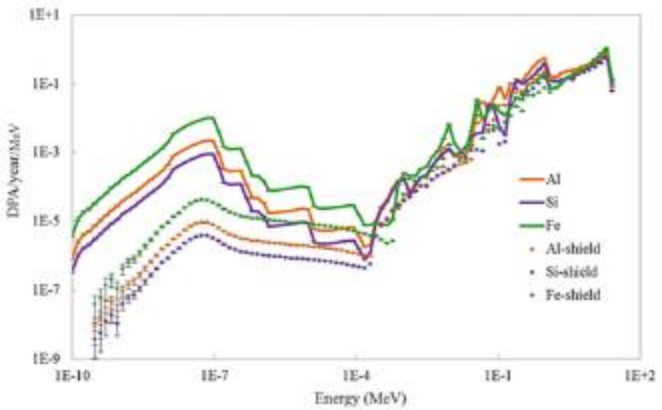

Fig. 8 BP5 DPA rate per unit energy versus neutron energy on the shell/cladding of the robot. Absolute errors are shown, which are the product of the relative error (i.e. fractional 1-sigma estimated uncertainties in the tally mean) and the calculated value.

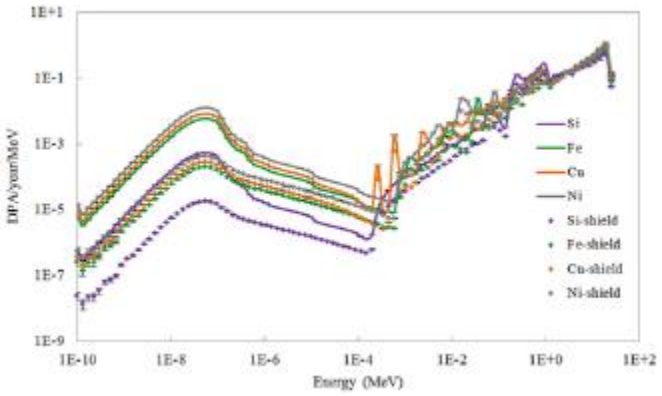

Fig. 9 BP5 DPA rate per unit energy versus neutron energy on the interior of the robot. Absolute errors are shown, which are the product of the relative error (i.e. fractional 1-sigma estimated uncertainties in the tally mean) and the calculated value.

Table 4 BP5 flux and DPA rate spectrum for different energy groups. The percent contribution is given by %f.

					DPA rate spectrum			
Energy group			Flux spectrum		Al shell no shield		Al shell shield	
MeV			n/cm^2/s	%f	year^{-1}	%f	year^{-1}	%f
0	to	2.5*e*-8	6.15*E*-05	8	4.63*E*-03	0.07	1.90*E*-05	0.0004
2.5*e*-8	to	4*e*-7	3.77*E*-04	49	1.18*E*-02	0.2	6.47*E*-05	0.002
4*e*-7	to	1*e*-6	1.35*E*-05	2	2.10*E*-04	0.003	8.44*E*-06	0.0002

					DPA rate spectrum			
Energy group			Flux spectrum		Al shell no shield		Al shell shield	
MeV			n/cm²/s	%f	year⁻¹	%f	year⁻¹	%f
1*e*-6	to	1*e*-5	2.87*E*-05	4	1.95*E*-04	0.003	1.96*E*-05	0.0005
1*e*-5	to	1	2.05*E*-04	27	2.07	33	8.62*E*-01	20
1	to	20	8.56*E*-05	11	4.11	66	3.45	80
Total			7.71E-04	100	6.19	100	4.31	100
					DPA rate spectrum			
Energy group			Flux spectrum		Si inner no shield		Si inner shield	
MeV			n/cm²/s	%f	year⁻¹	%f	year⁻¹	%f
0	to	2.5*e*-8	6.15*E*-05	8	1.39*E*-03	0.04	4.83*E*-05	0.002
2.5*e*-8	to	4*e*-7	3.77*E*-04	49	3.01*E*-03	0.08	1.20*E*-04	0.004
4*e*-7	to	1*e*-6	1.35*E*-05	2	6.70*E*-05	0.002	1.19*E*-05	0.0004
1*e*-6	to	1*e*-5	2.87*E*-05	4	8.86*E*-05	0.002	2.04*E*-05	0.0007
1*e*-5	to	1	2.05*E*-04	27	1.01	26	4.69*E*-01	16
1	to	20	8.56*E*-05	11	2.88	74	2.38	84
Total			7.71*E*-04	100	3.89	100	2.85	100

From Table 4 it may be observed that the greatest contribution to DPA rate on the Al shell of the robot corresponds to the fast flux (with 66% of the total) and the slow to intermediate group (with 33%). These contributions together (i.e. slow to fast neutrons) correspond to less than half of the fraction of the total flux (38%) where the contribution due to the thermal to epithermal flux is 49% of the total flux. Because the major damage effects are cause mainly by fast neutrons, it may be useful to use a fast neutron absorber such as boron carbide as a shielding material instead of the typical thermal neutron absorbers for this application (Braceyet al, 2004). However, it would be far less practical to completely surround the robot with boron carbide than compared to polyethylene. Therefore, boron carbide could be used as a supplemental standalone shield that is separate from the robot.

In Fig. 10, level curves of the DPA rate on the inner surface of the robot are plotted at the level corresponding to the maximum detected with MCNP for BP5. The mid plane of the robot is at the corresponding

(0,0,0) coordinates. The x-y axis view in Fig. 10 represents a top-down view of the robot. One can see from these level curves that the highest DPA rates in the robot occur at locations closest to the neutron beam. Peaks in the DPA rates occur in the exterior of the robot. As neutrons penetrate the robot, the DPA rate gradually decreases as the exterior and interior components of the robot attenuate the neutrons based on neutron transport theory. The added borated polyethylene shielding is shown to reduce DPA rates by approximately a factor of two.

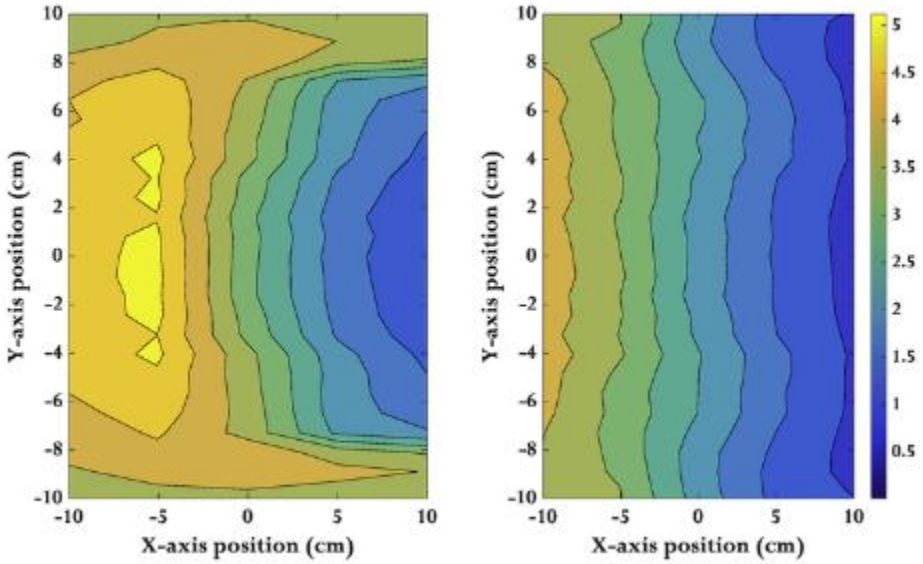

Fig. 10 BP5 x-y axis view. Rate of DPA/year on the inner surface of the robot without shielding (left) and with borated polyethylene shielding (right). The average relative error is 4.6% and 5.4% for the no shield and with shield configurations respectively. This is a top-down view of the robot with the neutron beam coming from the left to the right of the figures. The radius of the interior of the robot is 4 cm and the radius of the entire robot (interior and exterior) is 8 cm.

4 Conclusions

DPA rates in a robot were calculated using MCNP. Calculating the DPA for irradiated materials in a particular facility requires knowledge of the neutron spectrum as well as specific information about displacement damage in that material. The methods demonstrated in this paper can be applied to determine the radiation damage to robots and other objects in other radioactive environments and applications. MCNP has powerful tools for evaluating a wide range of reaction rates, and can generate common and uncommon design products (including DPA rates) with relatively straightforward input. DPA calculations are important across nuclear engineering, as they determine how the service life of tools and components, such as the robot analyzed in this work, are affected by radiation exposure. The results here can be compared to other data to determine if the DPA rate is acceptable, or will limit the robot's use.

For comparison, the DPA rates determined in this work are similar to those found in thermal reactor materials (Heinisch, 2004), which is expected since the TRIGA reactor is a thermal reactor. However, a more methodical study is needed to define the robot failure, and then find the DPA for the corresponding neutron fluence and energy spectrum that caused the robot to fail.

Rates of approximately 3–6 DPA/year were shown to occur in the robot; however the robotic imaging system would have a relatively low duty factor as it would actively only be in use on the order of minutes per day on average instead of the entire year. For this particular neutron imaging application, there will be days where the robot is in use for 1–2 h but other days where the robot use is minimal. In comparison, the duty cycle for reactor vessels is nearly 1. Since the duty cycle for the imaging system compared to a reactor vessel, the results of this paper could also be represented in terms of DPA/hours with beam-on. For example, the determined

3 to 6 DPA/year result could be expressed as 0.34 to 0.68 DPA/1000 h of beam-on use. The robot's gripper will receive the highest dose, since it is the part of the robot that is the closest to the beam; however, the gripper is easily replaceable and can be replaced before it fails.

Also, based on the results, a low-Z material such as polyethylene or water will provide the most effective neutron shielding. However, a fast neutron absorber, such as boron carbide, will be tested as a potential shielding material in the future to supplement the polyethylene shielding around the robot. One recommendation would be to use shielding for all robot stow locations. For example, after completing a radiograph, and while the radiation source is still on, have a shielded area that the robot can "hide" behind. Another recommendation would be to use radiation hardened components for the robot's End-of-Arm Tooling (EOAT), which would receive the highest dose since it is the part of the robot that would be the closest to the beam center location. One could also remotely replace the most sensitive electronic components of the robot since radiation damage imposes limitations in terms of operating lifetime. The improvements will benefit ongoing analysis efforts for radiation damage studies in industrial robots.

Acknowledgements

The first author wishes to thank Steve Biegalski and the generous support of the NETL staff for their help with the neutron imaging and Evan Harms for his help with the MCNP deck.

References

ANDOR Technology, Hardware Guide IXonEM, Version 1.22008 www.andor.com.

Applied Scintillation Technologies, SECUREX-ND, 2014 http://www.appscintech.com/products/securex-nd.

Blakeman E.D. and Bucholz J.A., Calculation of Dpa Rates at the HPIR HB-2 Beam Tube Nozzle Corner Using Three-dimensional Discrete Ordinates and Monte Carlo Models, TM-2003/2132004, Oak Ridge National Laboratory.

Bracey W., et al., Neutron absorber Qualification and acceptance testing from the Designer's Perspective,Berlin, GermanyIn: *14th Int. Symp. On the Packaging and Transportation of Radioactive Materials*,2004.

DOE, Robotics Technology Development Program Robotics 5-Year Plan, DOE/CE-0007T**vols. 1–3**, 1990,Environmental Restoration and Waste Management; Washington.

Gilbert M.R., et al., Neutron-induced dpa, Transmutations, Gas production, and Helium embrittlement of Fusion materials, *J. Nucl. Mater.* **442** (1–3), 2013, S755–S760.

Goorley T., James M., Booth T., Brown F., Bull J., Cox L.J., Durkee J., Elson J., Fensin M., Forster R.A.,Hendricks J. , Hughes H.G., Johns R., Kiedrowski B., Martz R., Mashnik S., McKinney G., PelowitzD., Prael R., Sweezy J. , Waters L., Wilcox T. and Zukaitis T., Initial MCNP6 Release Overview,*Nucl. Technol.* **180**, 2012, 298–315.

Heinisch H., Displacement damage in silicon carbide irradiated in Fission reactors, *J. Nucl. Mater.* 2004,175–181.

Houssay L.P., Robotics and Radiation Hardening in the Nuclear Industry, 2000, Diss. U of Florida.

Kobayashi T., et al., Effect of Calcium on mechanical properties of Recycled aluminum Casting alloys,*Mater. Sci. Technol.* 1997, 497–502.

Mascitti J.A. and Madariaga M., Method for the Calculation of DPA in the Reactor Pressure Vessel of Atucha II, **vol. 2011**, 2011, Science and Technology of Nuclear Installation.

Nagatani K., et al., Emergency response to the nuclear accident at the Fukushima Daiichi nuclear power plants using Mobile Rescue robots, *J. Field Robotics* **44–63**, 2012.

Nieves E., E-Mail Interview, 2013.

Olander D., Fundamental Aspects of Nuclear Reactor Elements, 1975, U.S. Dept. of Energy.

PyNE, ACE Cross Sections, 2016 http://pyne.io/usersguide/ace.html.

Risner J.M. and Blakeman E.D., Analysis of dpa rates in the HFIR reactor vessel using a Hybrid Monte Carlo/Deterministic method, *EPJ Web Conf.* **106**, 2016.

Shultis J. and Faw R., 2011, "An MCNP Primer," Kansas State University.

Was G.S., Fundamentals of Radiation Materials Science, 2007, Springer; Berlin.

Wootan D., Dpa calculational Methodologies used in Fission and Fusion reactor materials applications, In: *5th High Power Targetry Workshop. Poster Session*, 2014.

YASKAWA, "SIA5D," Motoman Robotics, 2012 http://www.motoman.com/datasheets/SIA5D.pdf.

Young G.J., Development of a Thermal Neutron Imaging Facility for Real Time Neutron Radiography and Computed Tomography, 1998, Diss. U of Texas at Austin, 211.

Zinkle S., Impact of Radiation Damage on Materials for Nuclear Energy Systems, 2012, EFRC Summer School on Defects, Deformation and Damage in Structural Materials; Knoxville.

Footnotes

[1]For actual physical deployment of the robotic imaging system, the robot will not be placed directly in the beam path. However, the main goal of this work is to demonstrate a method for determining DPA rates in a robot exposed to a neutron flux. Thus having the robot directly in the beam path simply shows the worst-case scenario situation for this application.